Research Square

Preprints are preliminary reports that have not undergone peer review. They should not be considered conclusive, used to inform clinical practice, or referenced by the media as validated information.

Carbonatite melt pathways connect the deep mantle to Archean craton margins

Graham Heinson

Graham.Heinson@adelaide.edu.au

Adelaide University

David Baker

Adelaide University

Article

Keywords:

Posted Date: October 16th, 2026

DOI: https://doi.org/10.21203/rs.3.rs-11239830/v1

License: This work is licensed under a Creative Commons Attribution 4.0 International License. Read Full License

Additional Declarations: No competing interests reported.

Carbonatite melt pathways connect the deep mantle to Archean craton margins

Graham Heinson[1], David Baker[1]

[1]School of Physics, Chemistry and Earth Sciences, Adelaide University, Adelaide SA 5001, Australia

Abstract

Earth's deep carbon-cycle has been active since subduction of carbon-rich oceanic crust began in the Paleoproterozoic. Petrological evidence for carbonatite melts suggests they are a significant part of the mantle carbon reservoir and act as a highly efficient, volatile-rich transporting agent that dissolve, mobilise, and transfer rare earth and sulphur-bearing elements from deep mantle into the crust at craton margins. However, direct geophysical imaging of carbonatite melts in the mantle are ambiguous as electrical resistivity and shear-wave velocity anomalies can also be ascribed to hydrous silicates in solid or small melt fractions. In this paper we use long-period MT data to image an electrically anisotropic and conductive (~1 Ohm.m) lower lithosphere (180 km depth) beneath the Archean core of the Gawler Craton in southern Australia. We interpret these features as metasomatically modified and channelised structures, potentially associated with carbon-bearing melts, where small fractions (~0.05 vol%) of carbonatite melt account for observed low resistivity. Additionally, low resistivity (<100 Ohm.m) regions are imaged at Moho depths in an arcuate belt around the Archean Craton, coincident with a shear-wave velocity decrease. Such low

resistivity regions are interpreted to be the signature of carbon exsolved as graphite from upward migrating deep-mantle carbonatite melts.

<u>199 words</u>

Introduction

It is well established that both organic and inorganic carbon is sequestered into the mantle by transport of oceanic sediment at subduction zones[1-4], with some fraction returned at island arc volcanics early in the subduction cycle[5]. However, a significant but unknown amount is transported deeper into the upper mantle in the form of carbonatites.[1,6], that have implications for mantle melting[7], lithospheric metasomatism[8,9], redox state[10], sulphur mobilisation[11-15], and rare earth element partitioning[2,16]. Carbon is eventually returned to the oceans and atmosphere at continental[17] and oceanic rifts[18]. The carbon cycle has been active since the Paleoproterozoic[19,20], but has changed with time[21] depending on the configuration of plate boundaries and fluctuations in carbon sequestration into the mantle.

From petrological studies, it has been shown that carbonatite melting in the mantle lowers the melting temperature of surrounding peridotite mantle by several hundred degrees and generates highly mobile, reactive melts that facilitate deep carbon cycling and promote chemical enrichment of the Earth's interior[13,22-24]. There is laboratory geophysical evidence that carbonatite melts at very small fractions (0.02-0.08 vol%) reduce the seismic shear-wave velocity[25] and significantly reduce (by up to three orders of magnitude compared to hydrous silicate melts of similar melt volume fraction) electrical resistivity[26-28]. However, direct geophysical observation of deep lithosphere shear-wave velocity and electrical

resistivity remains ambiguous as hydrous mantle phases, particularly phlogopite minerals that are fluorine rich, can also reduce shear wave velocity and electrical resistivity at comparable depths.[29,30].

In this paper we consider the causal mechanisms for low resistivity at the base of the Gawler Craton lithosphere and the case for carbonatite melt that has remained in situ since emplacement ~1.6 Ga. Previous studies have imaged a region of low electrical resistivity (< 100 Ohm.m) beneath the Archean part of the Gawler Craton, but the depth and vertical extent were not well resolved with only partial MT site coverage[31]. Forward model studies also suggest that the conductor potentially has anisotropic resistivity properties, but the degree and extent of anisotropic properties is not constrained[32]. Here we invert 200 long-period MT sites covering an area 640,000 km^2 over the Gawler Craton and Musgrave Province to reassess the resistivity, depth and geodynamic setting.

Geological and Geophysical Setting

The Gawler Craton is the major component of the South Australian Craton[33], as shown in **Figure 1**. The central part of the craton is Archean[34-36], surrounded by Paleoproterozoic orogenic belts[37-40]. The most significant tectonic event was the 1595 Ma Mesoproterozoic-aged eruption of the Gawler Range Volcanics[33,41,42], and the initial deposition of several iron-oxide copper gold (IOCG) deposits, most notable at Olympic Dam[41,43-45] at 1590 Ma. It has been suggested that both the Gawler Range Volcanics and the IOCG deposits are linked to an early Paleoproterozoic subduction event (1620 Ma) to the southwest of the current craton location. Initial arc-related melting occurred in the St Peter Suite[46-48], with the slab subducting beneath the Archean core of the Craton (comprising the Mulgathing and Sleaford

Complexes[34]). Several authors[43,49] have suggested that with high thermal fluxes in the Paleoproterozoic, subduction would have been shallow dipping and potentially the source of melt for the Gawler Range Volcanics and the thermal flux driving the IOCG formations.

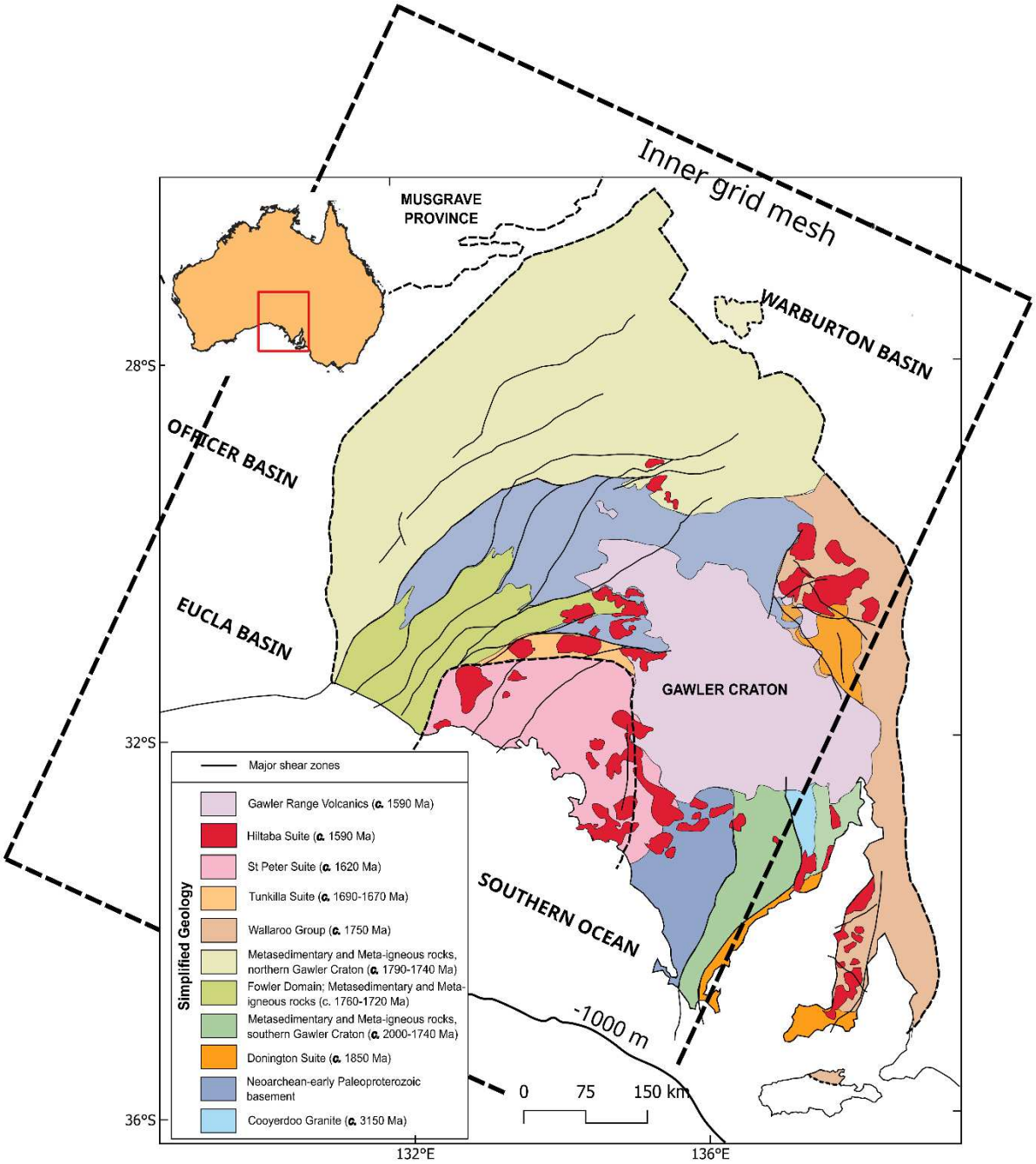

Figure 1. Broad-scale geological map of the Gawler Craton and Musgrave Province. The inner grid of the 3D model is shown by the dashed line, aligned 25° clockwise from

geographic north. The broader mesh extends 500 km beyond the inner grid as padding cells. Figure adapted from[47], re-drawn using Inkscape v1.2.1 (https://inkscape.org).

Understanding of the structure of the Archean core of the Gawler Craton is primarily defined by petrology of mantle xenoliths[50,51], and the geophysical imaging methods of seismic tomography[52-54], and magnetotellurics[31,43,55]. Analysis of >3000 mantle xenoliths across the craton suggested the lithosphere can be divided into a shallow Gawler Craton (60-130 km) representing the original cratonic core, and a deeper lithosphere (>160 km) that was added to the original core of the craton by Archean mantle plume interactions[50]. With high volumes of melt segregating volatiles, the lithosphere would initially be depleted lherzolite but has subsequent been metasomatized and refertilised by high temperature melts from the asthenosphere.

Seismic tomography[54] suggests that the lithosphere is about 180-200 km thick. From shear-wave splitting there is evidence[53,56] of anisotropy within the mid-lithosphere with a strike angle 68° $\pm$ 19° with a mean splitting time of 0.80 ± 0.29 s, almost perpendicular to the current plate motion[56]. A preliminary electrical resistivity model of the Gawler Craton using a long-period MT array prior to the establishment of the AusLAMP program highlighted a region of low resistivity of <100 Ohm.m at >80 km depth[31,43]. Further analysis using additional AusLAMP data across the southern Gawler Craton placed the conductor at >120 km, and forward modelling suggested that it is likely anisotropic, with a strike of about 130°[57]. The cause of low electrical resistivity in the upper mantle was suggested to be hydrated phlogopite, possibly enhanced by fluorine to be stable at higher temperatures[55,58,59].

Results

Magnetotelluric data were acquired at approximately 200 sites across the study region. Most sites form part of the Australian Lithospheric Architecture Magnetotelluric Project (AusLAMP) dataset[32,55], supplemented by additional legacy stations[31,60]. The data typically span periods from 10 to 10,000 s and include measurements of both impedance tensor and vertical magnetic field transfer functions.

Figure 2a shows phase tensors at a period of 21 s, coloured by minimum phase; additional data plots are shown in the Supplementary section Fig. S1 and Fig. S2. Black lines indicate major crustal boundaries[61]. At these relatively short periods, pronounced spatial variations in the phase response are evident across the study area. The Officer and Eucla Basins in the west are generally characterised by lower phase angles than the Musgrave Province to the north, whereas the Gawler Craton exhibits a more heterogeneous response.

At a longer period of 215 s (Fig. 2b), the phase tensors define a more spatially coherent pattern. The Musgrave Province and Gawler Craton are characterised by relatively high phase angles, contrasting with the lower phase angles observed across the Officer, Eucla and Warburton basins. Pronounced and systematically aligned phase-tensor ellipticity occurs along several major crustal boundaries, particularly the margins of the Gawler Craton and Musgrave Province. These patterns indicate strong lateral resistivity gradients associated with the boundaries between the major crustal domains[61].

The vertical magnetic field response at a period of 1,000 s is shown in Fig. 2c. Black induction arrows represent the real (in-phase) component and are reversed according to the Parkinson convention such that they point towards regions of low resistivity. Blue arrows represent the imaginary (quadrature-phase) component. The real induction arrows generally point away

from the comparatively resistive Musgrave Province and Gawler Craton, towards the surrounding Proterozoic belts, as well as towards the ocean to the south. The induction-arrow pattern is, however, spatially complex, reflecting substantial lateral variations in electrical resistivity along and across the major crustal boundaries.

At the longest period shown (2,154 s; Fig. 2d), the phase-tensor response becomes more spatially homogeneous, consistent with sensitivity to greater mantle depths. Nevertheless, the Gawler Craton remains characterised by relatively high phase angles, indicating a distinct deep resistive structure compared with the surrounding regions. Systematic alignment of the phase tensors with major crustal boundaries remains evident, particularly around the margins of the Gawler Craton, although this relationship is less pronounced around the Musgrave Province. Collectively, the phase-tensor and vertical-field responses demonstrate that the major crustal domains and their boundaries exert a strong influence on the regional

electrical structure over a broad range of depths.

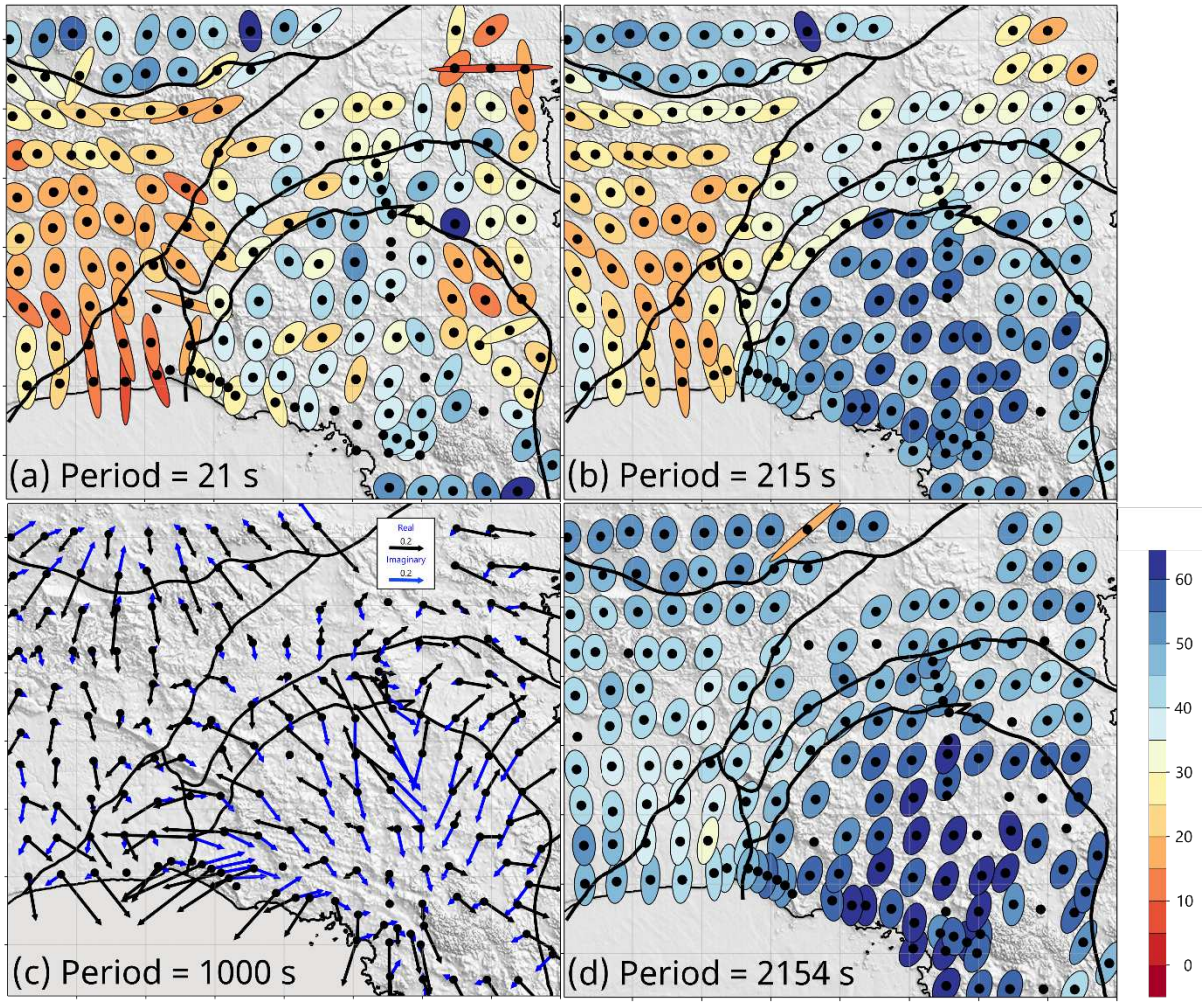

Figure 2. Phase tensors across the study area, coloured my minimum phase, at periods of (a) 21 s, (b) 215 s, and (d) 2,154 s. Induction arrows in the Parkinson convention, are shown for a period of 1,000 s. Thicker black lines represent major crustal boundaries[61]. All figures were produced using Viridien Geotools v.4.0.6.12598 (https://www.viridiengroup.com/expertise/multiphysics-imaging/geotools) and Inkscape v1.2.1 (https://inkscape.org).

All MT data were inverted to obtain a 3D model of electrical resistivity across the study region. The model grid was oriented 25° clockwise from geographic north as shown in Fig. 1,

extending farther south to incorporate the continent–ocean boundary. Details of the inversion procedure, model parameterisation and assessment of model fit are provided in the Methods section.

At 5 km depth (Fig. 3a) the model shows a clear distinction between the comparatively resistive Gawler Craton and Musgrave Province and the more conductive Eucla, Officer and Warburton basins. This contrast broadly follows the boundaries of the major crustal domains and demonstrates the strong influence of shallow sedimentary basins on the regional electrical structure. At 15 and 25 kms depth in Fig. 3b and 3c, the Gawler Craton becomes substantially more resistive, locally reaching values >10,000 Ohm.m. More conductive structures are locally evident within the middle crust, including beneath the IOCG Cairn Hill, Prominent Hill and Olympic Dam mines, consistent with conductive crustal features identified in previous MT studies[55,62].

In the lower crust, at 35 km depth (Fig. 3d) two major conductive regions are evident, parallel to the margin of the northeastern Gawler Craton, and additionally to the west of the Archean core of the Craton. Both conductors are within the wider Paleoproterozoic margin of the Craton. Conductive features remain evident at approximately 45 km depth (Fig. 3e), extending to depths near or below the Moho which is approximately 35-40 km[63] under the Gawler Craton.

In contrast, the upper mantle at 75-125 kms depth (Fig. 3f and Fig. 3g) is comparatively homogeneous, with only moderate variations in resistivity, predominantly between approximately 100 and 1,000 Ohm.m. Some of this subdued spatial variability probably reflects the smooth-model regularisation imposed during inversion rather than resolvable lithospheric structure.

A major change in electrical structure occurs at approximately 175 km depth (Fig. 3h), near the inferred base of the lithosphere, where a pronounced conductive anomaly is imaged beneath the Archean core of the Gawler Craton. The anomaly is ~10 Ohm.m, representing a decrease of two to three orders of magnitude relative to the overlying lithospheric mantle, and has been noted from previous models and inversions[31,32], although the depth from smaller arrays of MT sites could only be constrained to be >130 km. A similar low resistivity region has been imaged beneath the Superior Craton in Canada[64] and the Rio de la Plata Craton in Brazil[65]. This conductive structure is less evident at 225 km depth (Fig. 3i), where the model returns to a more spatially homogeneous resistivity distribution. The vertical confinement of this anomaly therefore indicates a discrete conductive layer or region near the lithosphere–asthenosphere boundary beneath the Gawler Craton, rather than a conductor extending continuously into the deeper mantle.

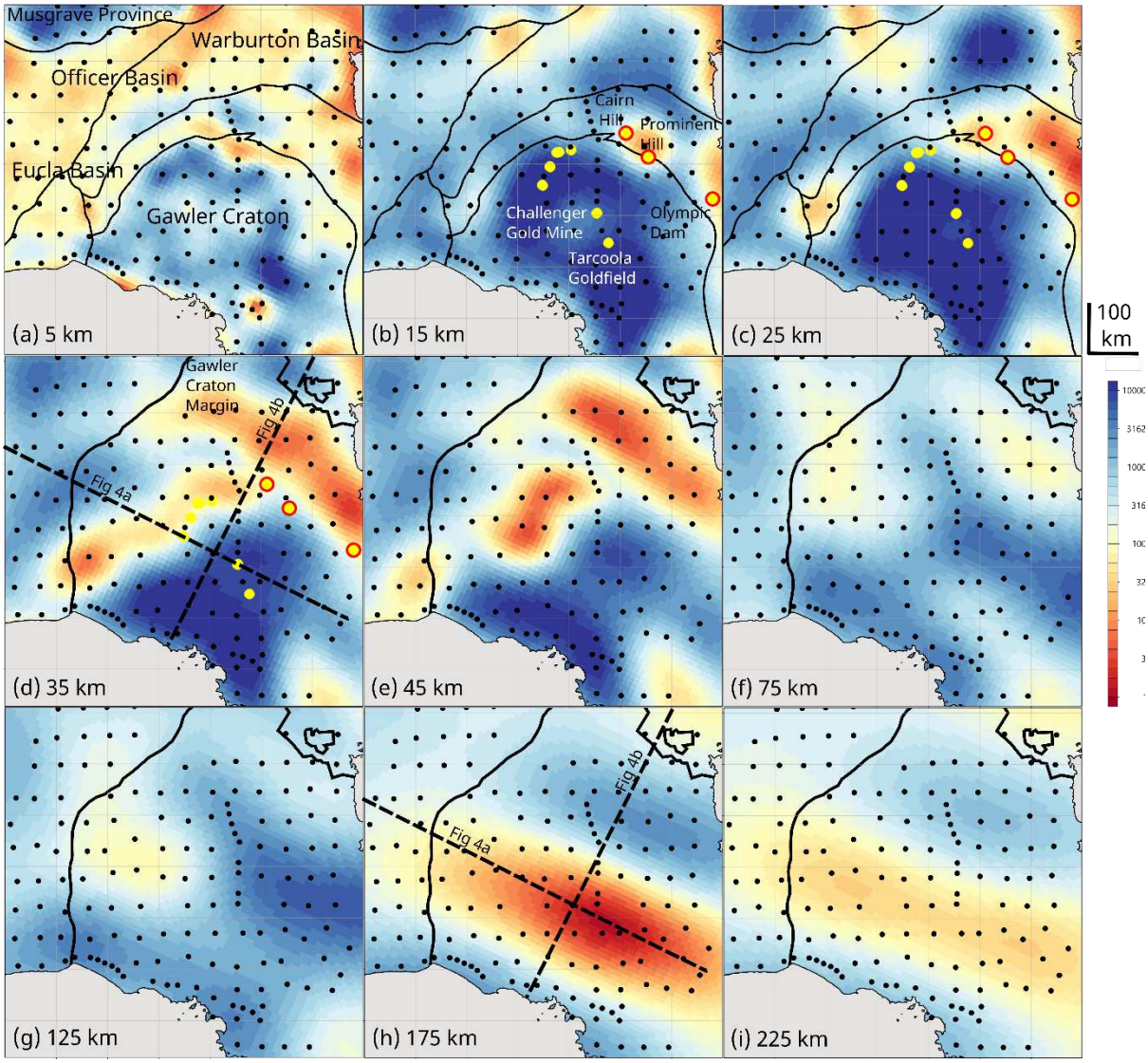

Figure 3. Three-dimensional isotropic resistivity model slices for depths ranging from 5-225 km. At upper crustal depth (5-25 km) major crustal boundaries are shown by thick black lines[61]. All figures were produced using Viridien Geotools v.4.0.6.12598 (https://www.viridiengroup.com/expertise/multiphysics-imaging/geotools) and Inkscape v1.2.1 (https://inkscape.org).

Two resistivity cross-sections extracted from the 3D model are shown along the profiles located in Fig. 3d and Fig. 3h. The first profile (Fig. 4a) extends approximately 800 km from northwest to southeast, crossing from the margin into the central part of the Gawler Craton.

The section is displayed with a vertical exaggeration of two. Superimposed on the resistivity model are contours of shear-wave velocity anomalies[54], expressed in m s^{-1}. Within the crust, velocity anomalies are calculated relative to the CRUST2.0 reference model[66], whereas below 40 km depth they are referenced to the mantle velocity model[67] . Regions of anomalously high and low shear-wave velocity anomalies are denoted by H and L, respectively.

The most prominent mantle conductor has a resistivity of approximately 10 Ohm.m and occurs directly beneath the region of highest shear-wave velocity. Importantly, the conductor is concentrated near the lower boundary of this high-velocity region, where the vertical shear-wave velocity gradient is greatest. A secondary conductive structure is evident near the base of the crust at approximately 40 km depth. This conductor spatially coincides with a pronounced low-velocity anomaly, where shear-wave velocities are reduced by approximately 250 m s^{-1} relative to the reference model. Figure 4b shows an approximately orthogonal, 600-km-long transect, also displayed with a vertical exaggeration of two. A similar relationship between electrical resistivity and seismic velocity is observed. The principal mantle conductor occurs beneath the high-velocity lithospheric anomaly and is again concentrated near the region of greatest velocity gradient towards its lower boundary. The conductivity decreases with increasing depth below this feature. A separate low-resistivity structure is evident within the crust and coincides with a shear-wave velocity reduction of approximately 250 m s^{-1}.

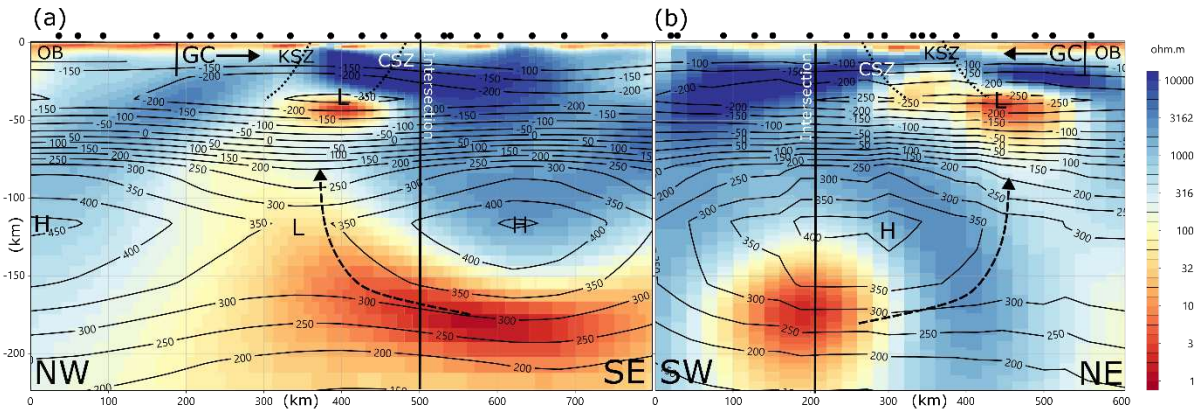

Figure 4. Cross-sections of resistivity models in Figs 3d and 3h, along with shear-wave velocity anomalies[54] as contours. Projected dip of major shear zones interpreted from seismic data[68], including the Karari Shear Zone (KSZ) and Coorabie Shear Zones (CSZ)[69-71], are superimposed on the section. The mapped margin of the Gawler Craton (GC) lies outside the principal conductive structure, indicating that the deep electrical boundary does not correspond directly with the mapped crustal boundary. Dashed lines indicate possible melt migration pathways from sub-lithosphere to underplating at Moho depths. All figures were produced using Viridien Geotools v.4.0.6.12598 (https://www.viridiengroup.com/expertise/multiphysics-imaging/geotools) and Inkscape v1.2.1 (https://inkscape.org).

Previous studies of lower-lithosphere resistivity anomalies beneath the Slave Craton and Gawler Craton suggested that structures causing low resistivity are anisotropic in nature[32,64] due to channelized flow from metasomatizing fluids and melts from the asthenosphere. We have undertaken a new anisotropic 3D inversion of the MT responses in Fig. 2; details of methodology and parameterisation are provided in the Methods section. The inversion solves for three orthogonal resistivity components within each model cell. The vertical resistivity (ρ_z) provides the reference component, while the two horizontal components (ρ_x

and ρ_y) are permitted to differ from ρ_z by up to a factor of 10. This limit is an imposed regularisation constraint rather than a physically determined bound and was selected to prevent the anisotropic solution from departing excessively from the corresponding isotropic model. The anisotropic inversion retained the orientation of the original model grid, 25° clockwise from geographic north. Consequently, the x direction is oriented southwest–northeast (25° clockwise from geographic north) and the y direction northwest–southeast (115° clockwise). It is not computationally feasible to define an arbitrary angle of anisotropy, so the choice of coordinate frame was based on previous forward modelling[32] and the geometry of the conductor in Fig. 3h.

The anisotropic inversion was initiated using the final isotropic resistivity model, such that the resulting model represents a perturbation of the preferred isotropic solution rather than an independently derived anisotropic resistivity structure. The anisotropic inversion converged to an RMS data misfit of 1.45, compared with approximately 1.82 for the isotropic model, indicating an improved fit to the observed MT responses of 20%.

Figures 5a–c show the three resistivity components at 180 km depth. The southwest–northeast component (ρ_x; Fig. 5a) and vertical component (ρ_z; Fig. 5c) exhibit similar spatial distributions, with minimum resistivities of ~10 Ohm.m beneath the central Gawler Craton. In contrast, the northwest–southeast component (ρ_y; Fig. 5b) exhibits resistivities of 1 Ohm.m within the same region. Thus, the principal lower-lithospheric conductor identified in the isotropic inversion is strongly anisotropic, with electrical resistivity in the northwest–southeast direction approximately one order of magnitude lower than in the orthogonal horizontal direction.

The depth dependence of this anisotropy is illustrated by the ratio of the two horizontal resistivity components (ρ_x/ρ_y) at 140, 180 and 220 km depth (Fig. 5d–f). At 140 km depth, the magnitude of horizontal resistivity anisotropy is approximately a factor of three. The contrast increases substantially with depth, reaching a factor of ~10 at 180 km, before decreasing to less than a factor of three at 220 km depth. The strongest anisotropic response is therefore concentrated near 180 km depth and coincides spatially with the lower-lithospheric conductor identified in the isotropic model. The smooth regularisation applied during inversion will inevitably distribute anisotropic structure over a finite vertical interval, limiting the precision with which its upper and lower boundaries can be determined. The Supplementary section shows additional cross-sections (Fig. S3) and planar sections (Fig. S4) of the anisotropic resistivity model.

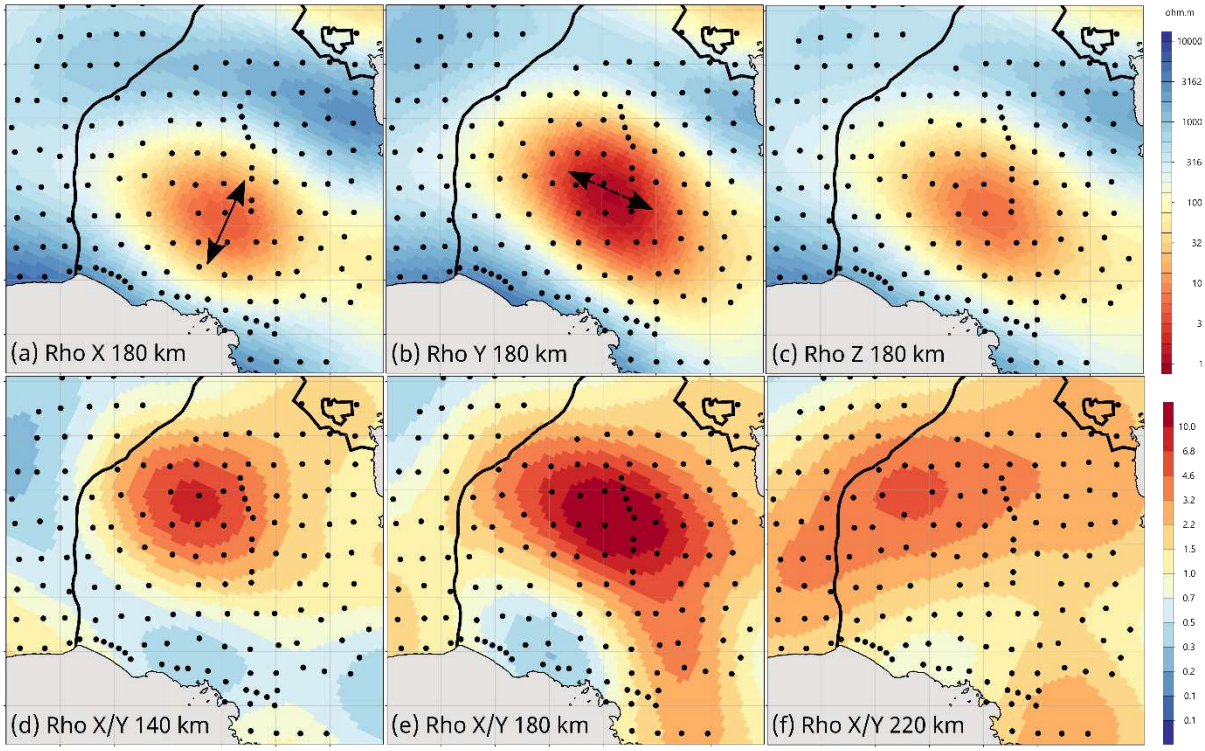

Figure 5. (a-c) Anisotropic resistivity at a depth of 180 km for three axes of orientation of resistivity; (d-f) Ratio of horizontal resistivity components at depths of 140, 180 and 220 km.

All figures were produced using Viridien Geotools v.4.0.6.12598 (https://www.viridiengroup.com/expertise/multiphysics-imaging/geotools) and Inkscape v1.2.1 (https://inkscape.org).

A reduction in RMS misfit by 20% for the anisotropic inversion does not, by itself, demonstrate that anisotropy is required by the data. To assess whether the improvement is systematic and associated specifically with the long-period responses that constrain the lower lithosphere, we compare the phase residuals (observed – model) for the off-diagonal impedance components (XY and YX) predicted by both isotropic and anisotropic models. Figure 6 shows the phase residuals at a period of 4,642 s, where the MT responses have substantial sensitivity to the deep lithospheric and sub-lithospheric electrical structure; additional phase residual plots at shorter periods are shown in the Supplementary section Fig. S5. Residuals within ±5° are shown in yellow, whereas increasingly positive and negative residuals outside this interval are represented by blue and orange–red colours, respectively.

For the isotropic model at 4,642 s, the XY and YX phase components display systematic residuals between the observed and modelled responses. Although there is spatial variability across the survey area, the residuals exhibit a coherent and opposing pattern between the two off-diagonal components, with XY phase residuals are commonly less than −5°, whereas YX phase residuals commonly exceed +5°. The complementary nature of these residual patterns indicates that the isotropic model is unable to simultaneously reproduce both horizontal components of the long-period MT response.

In contrast, the anisotropic model produces substantially smaller phase residuals for both the XY and YX components at 4,642 s. Across most of the study region, residuals fall within

±5°, and the systematic opposing residual pattern observed for the isotropic model is substantially reduced. The improvement is therefore not simply reflected in a lower global RMS misfit but occurs coherently in off-diagonal impedance components at long periods.

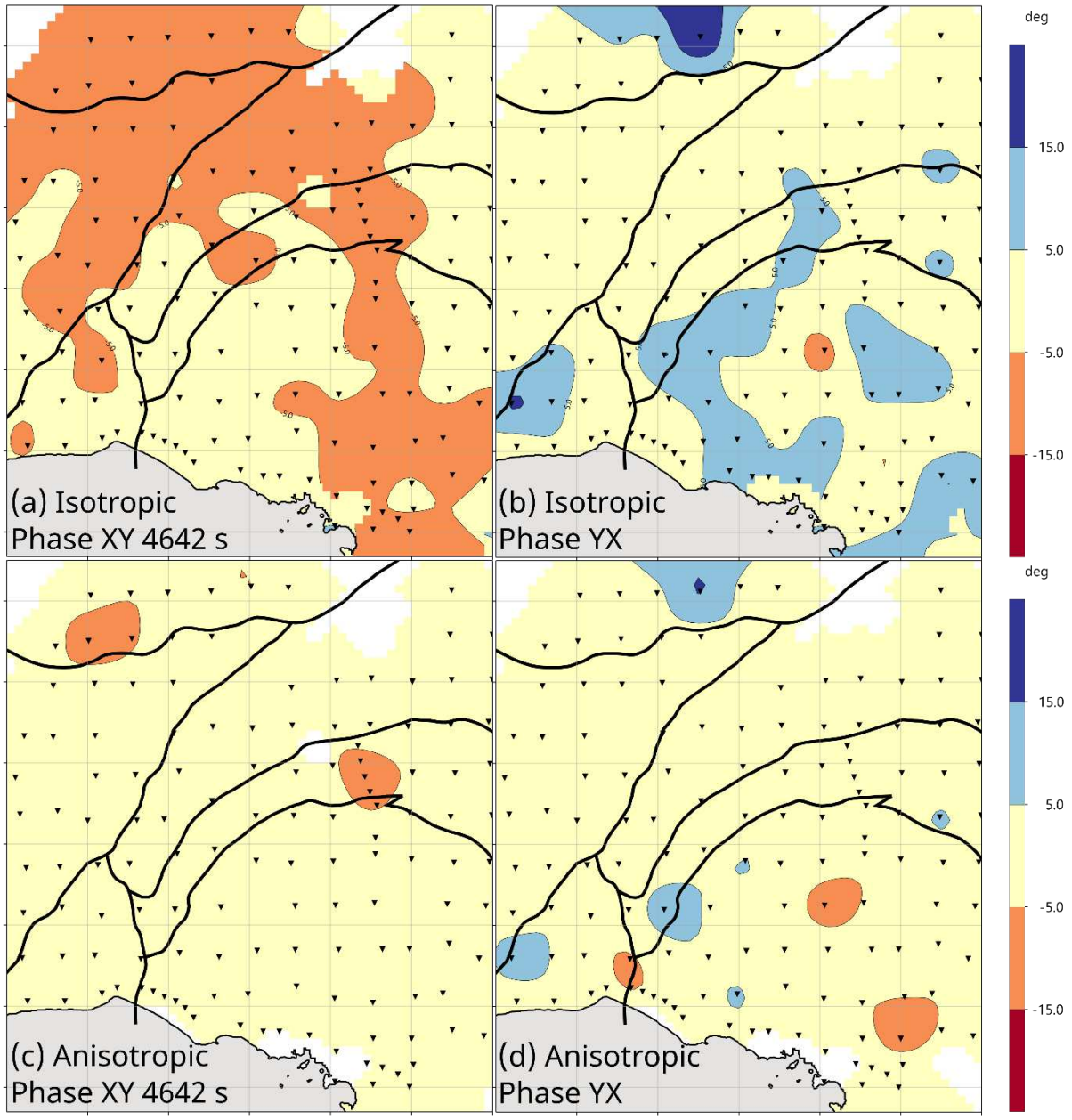

Figure 6. Phase residuals (observed – model) for the XY and YX components of the isotropic model (a, b) and the anisotropic model (c, d). All figures were produced using Viridien Geotools v.4.0.6.12598 (https://www.viridiengroup.com/expertise/multiphysics-imaging/geotools) and Inkscape v1.2.1 (https://inkscape.org).

Figure 7 compares depth profiles extracted from the 3D anisotropic resistivity model with predicted mantle resistivity profiles for the Gawler Craton and shear-wave velocity anomalies. The first profile in Fig. 7a is extracted from the central Gawler Craton, directly above the lower-lithospheric conductor. The three coloured curves represent the orthogonal components of the anisotropic resistivity model with ρ_y – blue, ρ_x -red and ρ_z - green. Predicted resistivity profiles are for a depleted lherzolitic mantle containing 0, 100 and 200 ppm H_2O[50,72]. Across much of the lithosphere above 150 km depth, the three resistivity components are similar and broadly consistent with the predicted resistivities of lherzolitic mantle containing 100–200 ppm H_2O. This correspondence is consistent with mantle xenolith observations[50], which suggest fertilisation or metasomatism of the Gawler Craton lithosphere associated with thermal and chemical flux from the underlying mantle. The resistivity profiles therefore indicate that the lithospheric mantle is unlikely to be represented by a completely dry lherzolitic composition, although resistivity alone cannot uniquely constrain mantle water content.

A pronounced departure from the predicted mantle resistivity profiles occurs at approximately 180 km depth. Here, the most conductive horizontal component ρ_y has a minimum of 1 Ohm.m, compared with approximately 5–10 Ohm.m for the orthogonal horizontal ρ_x and vertical ρ_z components. These values are substantially lower than predicted for the hydrated lherzolite models, demonstrating that hydration of nominally anhydrous mantle minerals alone is unlikely to account for the magnitude of the observed conductivity. The coincidence of the minimum resistivity with the maximum anisotropic contrast further indicates that the process responsible for the conductor has a strongly

directional electrical response. At shallower depths < 100 km the crust and mantle are otherwise highly resistive, of the order of 1,000–10,000 Ohm.m. In these regions, the magnitude of the resistivity is poorly constrained by MT data. Resistivity decreases rapidly towards the surface as a consequence of conductive sedimentary cover.

The pronounced decrease in resistivity at approximately 180 km depth also occurs near a reduction in shear-wave velocity. Although the seismic model does not resolve a discrete low-velocity layer coincident with the conductor, the low-resistivity region lies immediately beneath the highest shear-wave anomalous velocities, consistent with a relatively cold, thick and compositionally depleted cratonic lithosphere[50]. The electrical conductor is therefore concentrated near the lower boundary of the high-velocity lithospheric keel, rather than within its interior.

A second 1D profile extracted near the margin of the Gawler Craton in Fig. 7b shows a different relationship between crustal and mantle structure. Below the Moho, the three anisotropic resistivity components closely follow predicted resistivity profiles for hydrated lherzolitic mantle. This correspondence suggests that hydration and/or metasomatic modification may extend across a substantial region of the lithospheric mantle rather than being restricted to the central craton. The most prominent feature of the marginal profile, however, is a significant decrease in resistivity near the base of the crust at approximately 40 km depth. This conductor exhibits less electrical anisotropy than the lower-lithospheric anomaly beneath the central craton and coincides with a modest reduction in shear-wave velocity. The spatial correspondence between reduced resistivity and reduced seismic

velocity at the crust–mantle boundary provides independent evidence for modification of the lower crust and/or uppermost mantle along the margin of the Gawler Craton.

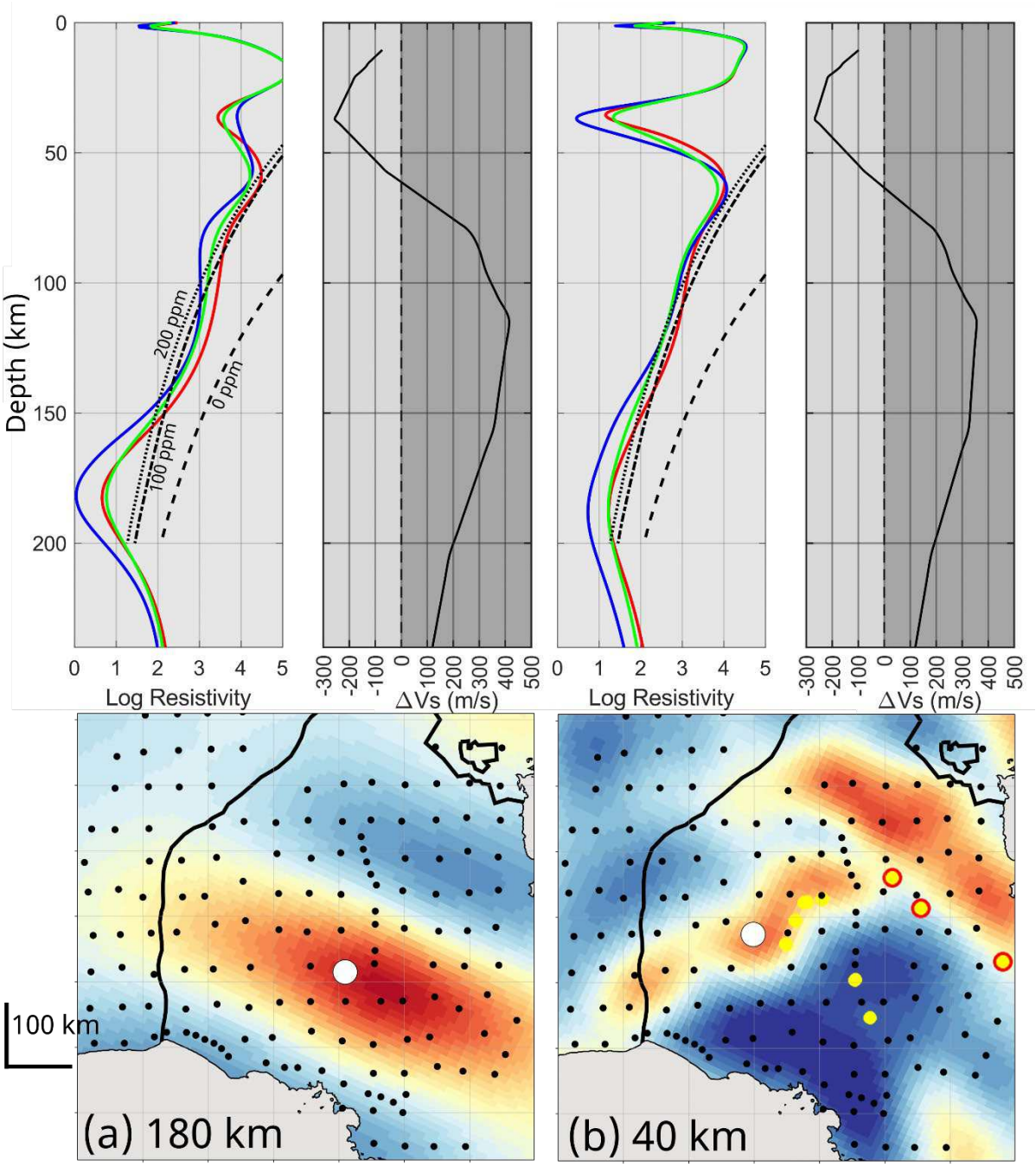

Figure 7. One-dimensional resistivity and shear-wave velocity models for sites (a) directly above the conductive lower-lithosphere, and (b) above the conductive crust-mantle at Moho depths along the margin of the Archean Gawler Craton. The three coloured curves

represent the orthogonal components of the anisotropic resistivity model with ρ_y – blue, ρ_x - red and ρ_z - green. Lherzolite mantle resistivity models for 0, 100 and 200 ppm H_2O are shown[72]. Anomalous shear-wave velocity models[54] are shown with fast anomalies > 0 m/s in the dark grey, and slow anomalies < 0 m/s in light grey. Figures were produced using Viridien Geotools v.4.0.6.12598 (https://www.viridiengroup.com/expertise/multiphysics-imaging/geotools), Matlab (R2021a https://matlab.mathworks.com/) and Inkscape v1.2.1 (https://inkscape.org).

Discussion

The anisotropic inversion reveals a pronounced low-resistivity region immediately beneath the seismically defined lithospheric keel of the Gawler Craton. At approximately 180 km depth, resistivity decreases to 1–10 Ohm.m and exhibits horizontal anisotropy approaching a factor of ten. In contrast, within the overlying lithosphere the observed resistivity is broadly consistent with moderately hydrated mantle containing approximately 100–200 ppm H_2O. This interpretation agrees with mantle xenolith studies[50,51], which indicate metasomatic modification of the depleted Archean core of the Gawler Craton and increasing hydration below approximately 100 km depth. The electrical structure therefore suggests a transition from a highly resistive cratonic interior to hydrated and metasomatically modified mantle at greater depths.

Hydration of nominally anhydrous mantle minerals alone, however, is insufficient to explain the exceptionally low resistivities observed at 180 km depth. An olivine-dominated mantle[73] is expected to have a resistivity of approximately 350 Ohm.m under relevant lithospheric

conditions. Increasing water content substantially enhances proton conduction and reduces mantle resistivity, but the predicted resistivities remain considerably higher than the observed values[74]. The minimum resistivity of 1 Ohm.m is more than an order of magnitude below that predicted for the hydrated mantle models considered here. An additional interconnected conductive phase is therefore required to explain the electrical observations.

One possible mechanism is the presence of hydrous minerals such as phlogopite[58,59,75]. Phlogopite is one of the few hydrous minerals stable in the upper mantle and may reduce bulk resistivity to approximately 10 Ohm.m and has a stability to a depth approaching 200 km under appropriate pressure, temperature and compositional conditions[30,76]. Fluorine substitution in phlogopite has also been proposed to further reduce electrical resistivity[58,59] fluorine-rich phlogopite-bearing mantle therefore cannot be excluded as a possible contributor to the observed conductor. However, relatively few laboratory measurements constrain the electrical properties of fluorine-bearing phlogopite at the pressures and temperatures appropriate to the base of cratonic lithosphere. Consequently, this mechanism is presently difficult to assess quantitatively.

An alternative explanation is the presence of a small fraction of interconnected carbonatite melt[26-28]. Carbonatite melts are exceptionally electrically conductive[26] and have substantially lower solidus temperatures than silicate mantle melts. Critically, carbonatite melts have favourable wetting properties in mantle mineral assemblages and can therefore form interconnected networks at very small melt fractions. Consequently, very small quantities of carbonatite melt can have a disproportionately large effect on bulk electrical resistivity.

Using SIGMELTS[77] for mantle resistivity parametrisation, we estimate that a carbonatite melt fraction of approximately 0.05 vol.% is sufficient to reduce bulk mantle resistivity to 1

Ohm.m under conditions appropriate to the base of the Gawler Craton lithosphere. The observed range of 1–10 Ohm.m can therefore be reproduced without requiring the large melt fractions normally associated with extensive silicate partial melting. At such low fractions, carbonatite melt may potentially persist within the mantle over long geological timescales[27].

The strong electrical anisotropy provides an additional constraint on the geometry of the conductive phase. The maximum anisotropy occurs at approximately the same depth as the minimum resistivity, suggesting that the conductor is preferentially interconnected in one horizontal direction. Metasomatism at the base of cratonic lithosphere may promote the migration and localisation of melts along fractures or grain-scale pathways controlled by lithospheric fabric and regional stress[17,78]. A comparable relationship has been proposed beneath the Superior Craton[64], with lower-lithospheric electrical anisotropy approaching an order of magnitude. The Gawler Craton observations are therefore consistent with small-volume conductive melt being preferentially interconnected along an anisotropic network near the base of the lithosphere. A cartoon schematic of the geological framework is shown in Figure 8, adapted from the cross-sections from Skirrow et al.[43]

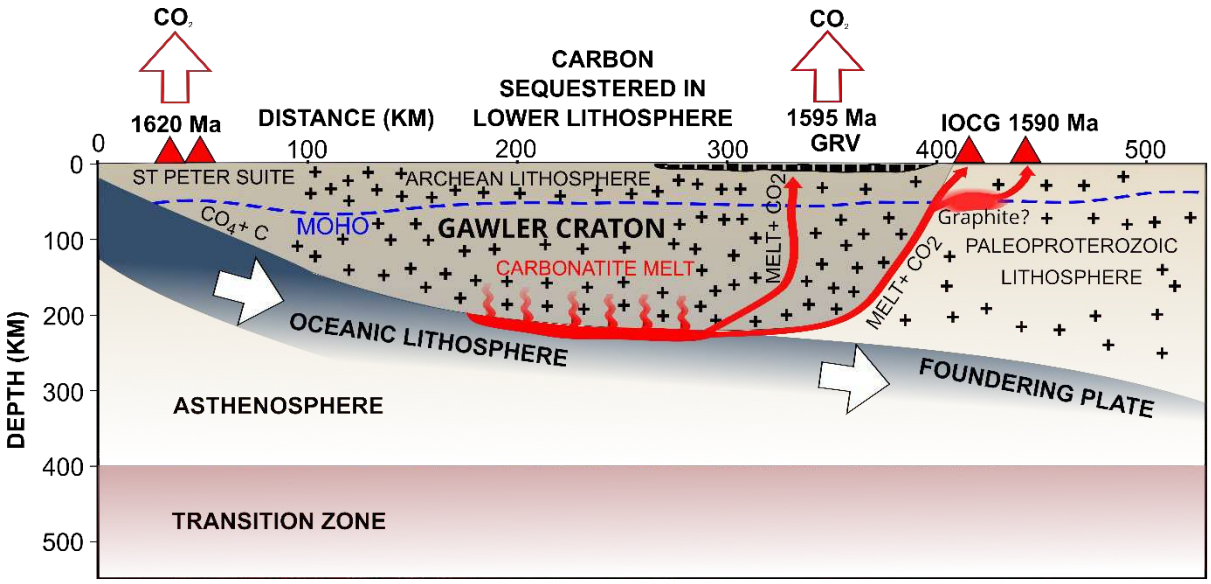

Figure 8. Schematic representation of a Paleoproterozoic subduction system beneath the Gawler Craton, from what is now southwest towards the northeast. Subduction is hypothesised to commence ~1620 Ma (forming arc magmatism in St Peter Suite), and at 1595-1590 Ma related to Gawler Range Volcanics (GRV) and IOCG mineralisation in the Olympic Domain. Carbonatite melt is present at the base of the Gawler Craton and potentially rises in channelised flow orthogonal to the plate subduction polarity. Figure adapted from[43].

The orientation of electrical anisotropy in the 3D inversion is defined by the coordinate system of the prescribed numerical model on the basis of previous forward-modelling studies[32] and the elongated geometry of the conductor at the base of the lithosphere, rather than being a free parameter. Shear-wave splitting (SKS) studies[53,56] identified a dominant seismic anisotropy beneath the South Australian Craton that is approximately orthogonal to the present-day direction of Australian plate motion, with a mean fast-axis orientation of the ~68° ± 19° relative to geographic north, and mean splitting is time of 0.95 ± 0.27 s. This

compares with the electrical anisotropy that has the higher resistivity at 25° relative to geographic north.

Rather than requiring agreement between the two observations, we suggest that this difference reflects distinct physical mechanisms operating at different depths within and beneath the cratonic lithosphere. The seismic anisotropy is interpreted to predominantly reflect deformation fabric frozen into the lithospheric mantle, whereas the strongest electrical anisotropy in our model occurs at approximately 180 km depth, close to or beneath the seismically defined base of the lithospheric keel. Electrical anisotropy may therefore reflect the geometry and connectivity of the conductive phase at the lithosphere–asthenosphere transition rather than the crystallographic fabric responsible for SKS splitting.

This distinction is consistent with the proposed presence of very small fractions of interconnected carbonatite melt. Electrical resistivity is exceptionally sensitive to the presence and connectivity of a highly conductive melt phase, such that melt fractions substantially below 0.1 vol.% can produce large changes in bulk resistivity. If carbonatite melt is preferentially distributed along aligned grain boundaries, fractures or other permeable pathways, it could generate strong electrical anisotropy without requiring a corresponding crystallographic fabric in the surrounding mantle. We suggest that seismic anisotropy primarily records inherited deformation within the cratonic lithosphere, whereas the deeper electrical anisotropy reflects preferential connectivity of a conductive phase, potentially carbonatite melt, near the base of the lithosphere.

Carbonatite melt also provides a potential mechanism for transferring carbon and other incompatible components from the asthenospheric mantle into the upper lithosphere[13,79], as shown in Fig. 8. We propose that the presently observed low melt fraction may represent

the residual expression of a system that previously contained larger volumes of carbon-rich melt. At higher melt fractions, carbonatite would be highly mobile[13] and could migrate laterally along the base of the cratonic keel before being focused towards its margins. Variations in lithospheric thickness, permeability and stress at craton margins could provide pathways for carbonatite and associated silicate melts and fluids to migrate into the overlying lithosphere.

The electrical structure surrounding the Archean Gawler Craton is consistent with such a mechanism. Conductive lower-crustal and uppermost-mantle regions approximately follow parts of the craton margin rather than the central Archean cratonic keel. These conductors are spatially associated with modest reductions in seismic shear-wave velocity. Although the seismic anomalies are comparatively weak, their spatial correspondence with the electrical structures provides independent evidence for modification of the lower crust and uppermost mantle around the craton margin.

Present-day aqueous or saline fluids are unlikely to provide a satisfactory explanation for persistent resistivities of 1–10 Ohm.m within the lower crust of a tectonically stable craton. Maintaining interconnected free fluids over geological timescales at depths of 35–45 km is problematic because fluids are expected to migrate, react with the surrounding rocks, or become incorporated into mineral phases. A more persistent conductive phase is therefore required.

Graphite precipitated from carbon-rich fluids provides one such mechanism, as shown in Fig. 8. Graphite is highly conductive when sufficiently interconnected and can remain stable over geological timescales and can precipitate from C–O–H fluids (comprising H_2O, CO_2 and CH_4 as the most important fluid species) as pressure, temperature and oxygen fugacity evolve

during migration through the lower crust[80-82]. Under conditions appropriate to the Gawler Craton of low heat flow (~50 $mW.m^{-2}$)[83] and low-geothermal gradient[50], graphite precipitation may be favoured at depths of approximately 35–45 km[81]. This depth range corresponds closely to the prominent lower-crustal conductors imaged around parts of the craton margin.

We therefore propose a linked mantle-to-crustal carbon system. Small fractions of carbonatite melt presently retained near the base of the lithosphere can account for the exceptionally low resistivity and strong anisotropy observed at approximately 180 km depth. During earlier periods of enhanced melt production, larger volumes of carbonatite and associated carbon-rich melts and fluids may have migrated laterally towards the margins of the Archean cratonic keel and subsequently ascended into the lithosphere. Progressive reaction and oxidation of these carbon-bearing fluids within the lower crust could have resulted in graphite precipitation, producing the persistent crustal conductors observed today. In this interpretation, the deep anisotropic conductor and the lower-crustal conductors represent different expressions of a long-lived carbon-rich metasomatic system extending from the base of the Gawler Craton lithosphere into its crustal margins.

Conclusion

We interpret the low resistivity at the base of the Gawler Craton as evidence for carbonatite melt concentrated near the lithosphere–asthenosphere boundary. We propose that Paleoproterozoic oceanic lithosphere was subducted beneath the craton from the southwest, introducing carbon-rich material that metasomatized the base of the lithosphere and generated anisotropic melt-filled structures. Along the craton margins, this carbonatite melt was mobilized into the lower crust, producing mafic underplating and the precipitation

of graphite, thereby creating conductive lower crustal zones. The close spatial association between these conductive pathways and major IOCG deposits suggests that carbonatite melts played an important role in their formation. We further propose that a small fraction of carbonatite melt has remained trapped beneath the lithosphere since approximately 1.6 Ga, preserving the highly conductive mantle signature observed today.

Methods

A database of 200 long-period (10-10000 s) MT responses was established from a combination of new AuLAMP sites[55] and legacy data[31,60] as shown in Fig. 2a-d, and in the Supplementary section Fig. S1 and S2. The sites cover an area of 800 km by 800 km, with a typical site spacing of 55 km.

Long-period MT sites were typically collected at 10 Hz for between 4-6 weeks, with either AuScope and Geoscience Australia LEMI 424 instruments with fluxgate sensors and two 50 to 100 m dipoles with Ag-AgCl electrodes, or with AuScope EarthData Loggers and Bartington Mag-03 fluxgate sensors, also with 50 m dipoles and Ag-AgCl of Pb-PbCl electrodes. Long-period MT response estimates in the frequency domain were obtained using the BIRRPS processing codes[84,85]. Additional data processing and editing were carried out using MTPy[86] and Viridien Geotools V.4.0.3.12574 (https://www.viridiengroup.com/expertise/multiphysics-imaging/geotools).

Three-dimensional inversions were carried out using Viridien Geotools v.4.0.6.12598 (https://www.viridiengroup.com/expertise/multiphysics-imaging/geotools) software based on the finite-difference forward modelling and a nonlinear conjugate gradient inversion

algorithm[87,88]. A grid of 112 by 125 cells was orientated 25° clockwise from geographic north, with a 10 km inner grid covering all sites in Fig. 2. Padding extending 500 km in each direction with a 20% increase in grid size with adjacent padding cells from the inner grid. Given the relatively small topographic gradients, topography was not modelled, however, ocean bathymetry was included. Vertically, the top layer from sea level was 5 m thick, increasing by 5% per cell with depth to 410 km, and then at 20% per cell with depth to 800 km, for a total of 179 vertical cells steps, and a total of ~2.5 million cells. The start model was 100 Ohm.m to 410 km depth, 10 Ohm.m from 410 - 670 km, and 1 Ohm.m below 670 km. The deeper mantle resistivities were included based on robust global satellite-derived models[89] and have the additional benefit of satisfying boundary conditions of negligibly small induced fields that are uniform below the transition zone.

The inversion used 16 periods, spaced evenly at 5 per decade from 10 s to 10000 s. Error floors were set at 5% on each of the four impedance components, and a fixed error floor of 0.02 for the vertical field. The inversion included an estimate of site-by-site local distortion, but a high weighting was used to allow the inversion to include variability mostly as resistivity in the subsurface. Horizontal smoothing (tauH) and vertical smoothing (tauV) were varied between 0.01 and 1; our preferred model with no bias between horizontal and vertical smoothing with tauH = tauV = 0.1. Near-surface smoothing to a depth of 500 m was included to ensure that modelled resistivities near the surface were uniform across the mesh, based on the premise that near-surface sedimentary layers are laterally extensive and continuous between sites.

Overall, after 50 iterations from the start model, the isotropic misfit had an RMS of 1.82. Model fits for apparent resistivity invariant and phase invariant are shown in the Supplementary Section Figure for periods of 21 s, 215 s and 2154 s; fits of the tipper magnitudes are also shown in Figure for periods of 215 s and 2154 s. Layer conductance models are shown in Supplementary Section Figure S1 for smoothing parameters tauH and tauV ranging from 1 to 0.01.

Anisotropic inversion was carried out using Viridien Geotools v.4.0.6.12598 (https://www.viridiengroup.com/expertise/multiphysics-imaging/geotools) software. The anisotropic inversion minimises misfit with the vertical component of resistivity ρ_z and then allows ρ_x and ρ_y to vary by up to a factor of 10 from ρ_z. The start model was the isotropic model, on the assumption that anisotropy is a perturbation of the isotropic model, rather than starting from a half space. After 50 iterations, the RMS was 1.45. Data misfits for isotropic and anisotropic models are shown in Fig. 6 and Supplementary Fig. S5.

Acknowledgements

The AusLAMP long-period MT data utilised in this study were funded and acquired through collaborative efforts involving Geoscience Australia, the Geological Survey of South Australia, Adelaide University, and AuScope. Instrumentation and software support were provided by Geoscience Australia and AuScope through the ANSIR network, with additional support from the Australian Government via the National Collaborative Research Infrastructure Strategy (NCRIS). We gratefully acknowledge the many individuals from these organisations whose field efforts over the past four decades made this study possible, as well as the communities

that provided access to land, particularly across remote and regional Australia. We also acknowledge the Traditional Custodians of the lands on which data acquisition was undertaken.

Author contributions

G. Heinson compiled the data sets, undertook modelling, data analysis and wrote the paper. D. Baker undertook modelling.

Data availability statement

The AusLAMP long-period magnetotelluric time series and higher-level products are archived at the National Computational Infrastructure under the AusLAMP collection (https://doi.org/10.25914/5eaa30cc934d0). The South Australian time series, from packed raw archives through level 1 and level 2 products, are available at https://doi.org/10.25914/bzd5-n780. South Australian state delivery is via SARIG (https://map.sarig.sa.gov.au/). Processed magnetotelluric transfer functions for the surveys used in this study are available through AusMT ([http://AusLAMP%20South%20Australia]https://ausmt.auscope.org.au), Australia's Magnetotelluric Data Portal, with provenance information and links to the original data sources provided for each survey. Elevation data were sourced from Geoscience Australia's Geophysical Archive Data Delivery System (https://portal.ga.gov.au/persona/gadds) released under a CC BY 4.0 license (https://www.ga.gov.au/copyright).

Figures were generated using Viridien Geotools, V.4.0.3.12574; Python v3.12.7 (https://www.python.org/), QGIS v3.34.3-Prizren (https://qgis.org), and Inkscape V1.2.1 (https://inkscape.org/cs).

Code availability statement

The custom scripts used in this study for data processing and visualization are available from the corresponding author upon reasonable request. Magnetotelluric numerical modelling was undertaken using using Viridien Geotools v.4.0.6.12598 (https://www.viridiengroup.com/expertise/multiphysics-imaging/geotools).

Additional Information (including a Competing Interests Statement)

The author(s) declare no competing interests.

Materials & Correspondence.

Correspondence and material requests should be addressed to Graham.Heinson@adelaide.edu.au

Figure legends (these are limited to 350 words per figure)

Figure 1. Broad-scale geological map of the Gawler Craton and Musgrave Province. The inner grid of the 3D model is shown by the dashed line, aligned 25° clockwise from geographic north. The broader mesh extends 500 km beyond the inner grid as padding cells. Figure adapted from[47], re-drawn using Inkscape v1.2.1 (https://inkscape.org).

Figure 2. Phase tensors across the study area, coloured my minimum phase, at periods of (a) 21 s, (b) 215 s, and (d) 2,154 s. Induction arrows in the Parkinson convention, are shown for a period of 1,000 s. Thicker black lines represent major crustal boundaries[61]. All figures were produced using Viridien Geotools v.4.0.6.12598 (https://www.viridiengroup.com/expertise/multiphysics-imaging/geotools) and Inkscape v1.2.1 (https://inkscape.org).

Figure 3. Three-dimensional isotropic resistivity model slices for depths ranging from 5-225 km. At upper crustal depth (5-25 km) major crustal boundaries are shown by thick black lines[61]. All figures were produced using Viridien Geotools v.4.0.6.12598 (https://www.viridiengroup.com/expertise/multiphysics-imaging/geotools) and Inkscape v1.2.1 (https://inkscape.org).

Figure 4. Cross-sections of resistivity models in Figs 3d and 3h, along with shear-wave velocity anomalies[54] as contours. Projected dip of major shear zones interpreted from seismic data[68], including the Karari Shear Zone (KSZ) and Coorabie Shear Zones (CSZ)[69-71], are superimposed on the section. The mapped margin of the Gawler Craton (GC) lies outside the principal conductive structure, indicating that the deep electrical boundary does not correspond directly with the mapped crustal boundary. Dashed lines indicate possible melt migration pathways from sub-lithosphere to underplating at Moho depths. All figures were produced using Viridien Geotools v.4.0.6.12598 (https://www.viridiengroup.com/expertise/multiphysics-imaging/geotools) and Inkscape v1.2.1 (https://inkscape.org).

Figure 5. (a-c) Anisotropic resistivity at a depth of 180 km for three axes of orientation of resistivity; (d-f) Ratio of horizontal resistivity components at depths of 140, 180 and 220 km. All figures were produced using Viridien Geotools v.4.0.6.12598

(https://www.viridiengroup.com/expertise/multiphysics-imaging/geotools) and Inkscape v1.2.1 (https://inkscape.org).

Figure 6. Phase residuals (observed – model) for the XY and YX components of the isotropic model (a, b) and the anisotropic model (c, d). All figures were produced using Viridien Geotools v.4.0.6.12598 (https://www.viridiengroup.com/expertise/multiphysics-imaging/geotools) and Inkscape v1.2.1 (https://inkscape.org).

Figure 7. One-dimensional resistivity and shear-wave velocity models for sites (a) directly above the conductive lower-lithosphere, and (b) above the conductive crust-mantle at Moho depths along the margin of the Archean Gawler Craton. The three coloured curves represent the orthogonal components of the anisotropic resistivity model with ρ_y – blue, ρ_x - red and ρ_z - green. Lherzolite mantle resistivity models for 0, 100 and 200 ppm H_2O are shown[72]. Anomalous shear-wave velocity models[54] are shown with fast anomalies > 0 m/s in the dark grey, and slow anomalies < 0 m/s in light grey. Figures were produced using Viridien Geotools v.4.0.6.12598 (https://www.viridiengroup.com/expertise/multiphysics-imaging/geotools), Matlab (R2021a https://matlab.mathworks.com/) and Inkscape v1.2.1 (https://inkscape.org).

Figure 8. Schematic representation of a Paleoproterozoic subduction system beneath the Gawler Craton, from what is now southwest towards the northeast. Subduction is hypothesised to commence ~1620 Ma (forming arc magmatism in St Peter Suite), and at 1595-1590 Ma related to Gawler Range Volcanics (GRV) and IOCG mineralisation in the Olympic Domain. Carbonatite melt is present at the base of the Gawler Craton and potentially rises in channelised flow orthogonal to the plate subduction polarity. Figure adapted from[43].

References

1 Hu, H., Zhang, L. F., Lan, C. Y. & Liu, Z. C. Petrological evidence for deep subduction of organic carbon to subarc depths. *Communications Earth & Environment* **4**, doi:10.1038/s43247-023-01085-w (2023).

2 Spandler, C., Merdith, A. S. & Griffin, A. Linking carbonatites, rare earth ores, and subduction-fertilized mantle lithosphere. *Science Advances* **12**, doi:10.1126/sciadv.aeb2942 (2026).

3 Ague, J. J. & Nicolescu, S. Carbon dioxide released from subduction zones by fluid-mediated reactions. *Nature Geoscience* **7**, 355-360, doi:10.1038/ngeo2143 (2014).

4 Plank, T. & Manning, C. E. Subducting carbon. *Nature* **574**, 343-352, doi:10.1038/s41586-019-1643-z (2019).

5 Kelemen, P. B. & Manning, C. E. Reevaluating carbon fluxes in subduction zones, what goes down, mostly comes up. *Proceedings of the National Academy of Sciences* **112**, E3997-E4006, doi:doi:10.1073/pnas.1507889112 (2015).

6 Humphreys-Williams, E. R. & Zahirovic, S. Carbonatites and global tectonics. *Elements* **17**, 339-344, doi:10.2138/gselements.17.5.339 (2021).

7 Dasgupta, R. & Hirschmann, M. M. Melting in the Earth's deep upper mantle caused by carbon dioxide. *Nature* **440**, 659-662, doi:10.1038/nature04612 (2006).

8 Chen, C. F. *et al.* Carbonated sediment recycling and its contribution to lithospheric refertilization under the northern North China Craton. *Chemical Geology* **466**, 641-653, doi:10.1016/j.chemgeo.2017.07.016 (2017).

9 Foley, S. F. Rejuvenation and erosion of the cratonic lithosphere. *Nature Geoscience* **1**, 503–510, doi:10.1038/ngeo193 (2008).

10 Gao, M. D., Wang, Y., Foley, S. F. & Xu, Y. G. Variable mantle redox states driven by deeply subducted carbon. *Science Advances* **11**, doi:10.1126/sciadv.adu4985 (2025).

11 Chowdhury, P. & Dasgupta, R. Sulfur extraction via carbonated melts from sulfide-bearing mantle lithologies - Implications for deep sulfur cycle and mantle redox. *Geochim Cosmochim Ac* **269**, 376-397, doi:10.1016/j.gca.2019.11.002 (2020).

12 Chen, C. *et al.* Sulfide-rich continental roots at cratonic margins formed by carbonated melts. *Nature (London)* **637**, 615-621, doi:10.1038/s41586-024-08316-w (2025).

13 Ezad, I. S. *et al.* Incipient carbonate melting drives metal and sulfur mobilization in the mantle. *Science Advances* **10**, eadk5979, doi:10.1126/sciadv.adk5979 (2024).

14 Xue, S. & Li, Y. The partitioning of chalcophile and siderophile elements (CSEs) between sulfide liquid and carbonated melt. *Geochim Cosmochim Ac* **388**, 94-113, doi:10.1016/j.gca.2024.11.019 (2025).

15 Blanks, D. E. *et al.* Fluxing of mantle carbon as a physical agent for metallogenic fertilization of the crust. *Nature Communications* **11**, 4342, doi:10.1038/s41467-020-18157-6 (2020).

16 Hou, Z., Liu, Y., Tian, S., Yang, Z. & Xie, Y. Formation of carbonatite-related giant rare-earth-element deposits by the recycling of marine sediments. *Scientific Reports* **5**, 10231, doi:10.1038/srep10231 (2015).

17 Foley, S. F. & Fischer, T. P. An essential role for continental rifts and lithosphere in the deep carbon cycle. *Nature geoscience* **10**, 897-902, doi:10.1038/s41561-017-0002-7 (2017).

18 Mather, B. R., Müller, R. D., Dutkiewicz, A. & Zahirovic, S. Carbon emissions along divergent plate boundaries modulate icehouse-greenhouse climates. *Communications Earth & Environment* **7**, 48, doi:10.1038/s43247-025-03097-0 (2026).

19 Liu, D. Y. *et al.* Paleoproterozoic deep carbon cycle recorded in carbonatites. *Precambrian Research* **417**, doi:10.1016/j.precamres.2024.107669 (2025).

20 Liu, Z. C. *et al.* The global deep carbon cycle started in the Paleoproterozoic Era. *Lithos* **510**, doi:10.1016/j.lithos.2025.108113 (2025).

21 McCammon, C. *et al.* Deep Earth carbon reactions through time and space. *American Mineralogist* **105**, 22-27, doi:10.2138/am-2020-6888CCBY (2020).

22 Pintér, Z. *et al.* Experimental investigation of the composition of incipient melts in upper mantle peridotites in the presence of CO2 and H2O. *Lithos* **396**, doi:10.1016/j.lithos.2021.106224 (2021).

23 Prelević, D. *et al.* Recent advances made by reaction experiments on melting of heavily metasomatized hydrous mantle. *Earth-Science Reviews* **256**, 104881, doi:https://doi.org/10.1016/j.earscirev.2024.104881 (2024).

24 Walter, M. J. *et al.* Primary carbonatite melt from deeply subducted oceanic crust. *Nature* **454**, 622-625 (2008).

25 Huang, Y. *et al.* Upper mantle low-velocity layer tied to volatile-charged carbonate melts. *Science Advances* **12**, eaec1018, doi:doi:10.1126/sciadv.aec1018 (2026).

26 Gaillard, F., Malki, M., Iacono-Marziano, G., Pichavant, M. & Scaillet, B. Carbonatite melts and electrical conductivity in the asthenosphere. *Science* **322**, 1363-1365, doi:10.1126/science.1164446 (2008).

27 Yoshino, T., Laumonier, M., McIsaac, E. & Katsura, T. Electrical conductivity of basaltic and carbonatite melt-bearing peridotites at high pressures: Implications for melt distribution and melt fraction in the upper mantle. *Earth and Planetary Science Letters* **295**, 593-602, doi:10.1016/j.epsl.2010.04.050 (2010).

28 Zhao, B., Zhu, J., Chen, Q. & Yoshino, T. Electrical conductivity of carbonatite melts to 20 GPa: Constraints on partial melting atop the 410-km discontinuity and in the lower mantle transition zone. *Journal of Geophysical Research: Solid Earth* **131**, e2025JB033390, doi:https://doi.org/10.1029/2025JB033390 (2026).

29 Sun, J., Yang, Y., Ingrin, J., Wang, Z. & Xia, Q. Impact of fluorine on the thermal stability of phlogopite. *American Mineralogist* **107**, 815-825, doi:10.2138/am-2022-8051 (2022).

30 Shu, C. T., Foley, S. F., Ezad, I. S., Daczko, N. R. & Shcheka, S. S. Experimental melting of phlogopite websterite in the upper mantle between 1.5 and 4.5 GPa. *J Petrol* **65**, doi:10.1093/petrology/egae030 (2024).

31 Thiel, S. & Heinson, G. Electrical conductors in Archean mantle; result of plume interaction? *Geophysical research letters* **40**, 2947-2952, doi:10.1002/grl.50486 (2013).

32 Tietze, K., Thiel, S., Brand, K. & Heinson, G. Comparative 3D inversion of magnetotelluric phase tensors and impedances reveals electrically anisotropic base of Gawler Craton, South Australia. *Exploration Geophysics* **55**, 575-601, doi:10.1080/08123985.2023.2281615 (2024).

33 Hand, M., Reid, A. & Jagodzinski, E. Tectonic framework and evolution of the Gawler Craton, Southern Australia. *Economic Geology* **102**, 1377–1395, doi:10.2113/gsecongeo.102.8.1377 (2007).

34 Reid, A. J. & Daly, S. J. The Mulgathing and Sleaford Complexes of the Gawler Craton; a historical perspective of the geology and mineral potential. *MESA journal* **52**, 4-12 (2009).

35 Dutch, R. A., Hand, M. & Kelsey, D. E. Unravelling the tectonothermal evolution of reworked Archean granulite facies metapelites using in situ geochronology: an example from the Gawler Craton, Australia. *Journal of Metamorphic Geology* **28**, 293-316, doi:10.1111/j.1525-1314.2010.00867.x (2010).

36 Hoatson, D. M. *et al.* Late Archean Lake Harris Komatiite, central Gawler Craton, South Australia; geologic setting and geochemistry. *Economic geology and the bulletin of the Society of Economic Geologists* **100**, 349-374, doi:10.2113/gsecongeo.100.2.349 (2005).

37 Armit, R. *et al.* Late Palaeoproterozoic evolution of the buried northern Gawler Craton. *Precambrian Research* **291**, 178-201, doi:10.1016/j.precamres.2017.01.023 (2017).

38 Halpin, J. A. & Reid, A. J. Earliest Paleoproterozoic high-grade metamorphism and orogenesis in the Gawler Craton, South Australia: The southern cousin in the Rae family? *Precambrian Research* **276**, 123-144, doi:10.1016/j.precamres.2016.02.001 (2016).

39 Stewart, J. R., Betts, P. G., Collins, A. S. & Schaefer, B. F. Multi-scale analysis of Proterozoic shear zones: An integrated structural and geophysical study. *J Struct Geol* **31**, 1238-1254, doi:10.1016/j.jsg.2009.07.002 (2009).

40 Swain, G. M., Hand, M., Teasdale, J., Rutherford, L. & Clark, C. Age constraints on terrane-scale shear zones in the Gawler Craton, southern Australia. *Precambrian Research* **139**, 164-180, doi:10.1016/j.precamres.2005.06.007 (2005).

41 Reid, A. J. & Hand, M. Mesoarchean to Mesoproterozoic evolution of the southern Gawler Craton, South Australia. *Episodes* **35**, 216-225, doi:DOI 10.18814/epiiugs/2012/v35i1/021 (2012).

42 Pankhurst, M. J., Schaefer, B. F., Betts, P. G., Phillips, N. & Hand, M. A Mesoproterozoic continental flood rhyolite province, the Gawler Ranges, Australia:

the end member example of the Large Igneous Province clan. *Solid Earth* **2**, 25-33, doi:10.5194/se-2-25-2011 (2011).

43 Skirrow, R. G., van der Wielen, S. E., Champion, D. C., Czarnota, K. & Thiel, S. Lithospheric architecture and mantle metasomatism linked to iron oxide Cu-Au ore formation: Multidisciplinary evidence from the Olympic Dam region, South Australia. *Geochemistry Geophysics Geosystems* **19**, 2673-2705, doi:10.1029/2018gc007561 (2018).

44 Skirrow, R. G. Iron oxide copper-gold (IOCG) deposits - A review (part 1): Settings, mineralogy, ore geochemistry and classification. *Ore Geology Reviews* **140**, doi:10.1016/j.oregeorev.2021.104569 (2022).

45 Skirrow, R. G. Iron oxide copper-gold (IOCG) deposits - A review (part 2): fluid, metal and sulfur sources and ore genesis. *Ore Geology Reviews* **189**, doi:10.1016/j.oregeorev.2026.107120 (2026).

46 Flint, R. B., Rankin, L. R. & Fanning, C. M. Definition; the palaeoproterozoic St. Peter suite of the western Gawler craton. *Geological Survey of South Australia Quarterly Geological Notes* **114**, 2-8 (1990).

47 Reid, A. J. *et al.* Resolving tectonic settings of ancient magmatic suites using structural, geochemical and isotopic constraints; the example of the St Peter Suite, southern Australia. *Australian journal of earth sciences* **67**, 31-58, doi:10.1080/08120099.2019.1632224 (2020).

48 Swain, G. *et al.* Petrogenesis of the St Peter Suite, southern Australia; arc magmatism and Proterozoic crustal growth of the South Australian Craton. *Precambrian research* **166**, 283-296, doi:10.1016/j.precamres.2007.07.028 (2008).

49 Betts, P. G. *et al.* Mesoproterozoic plume-modified orogenesis in eastern Precambrian Australia. *Tectonics* **28**, doi:10.1029/2008tc002325 (2009).

50 Sudholz, Z. J. *et al.* Multi-stage evolution of the South Australian Craton; petrological constraints on the architecture, lithology, and geochemistry of the lithospheric mantle. *Geochemistry, geophysics, geosystems* **23**, n/a, doi:10.1029/2022GC010558 (2022).

51 Selway, K., Özaydın, S. & Payne, J. Metasomatism and depletion of the southern Gawler Craton from combined mantle xenocryst and AusLAMP magnetotelluric data.

Exploration geophysics (Melbourne) **55**, 602-616, doi:10.1080/08123985.2023.2282711 (2024).

52 Eakin, C. M. Lithospheric architecture and mantle flow revealed by quasi-Love wave scattering beneath Australia. *Communications Earth & Environment* **2**, 276, doi:10.1038/s43247-021-00276-7 (2021).

53 Eakin, C. M., Davies, D. R., Ghelichkhan, S., O'Donnell, J. P. & Agrawal, S. The influence of lithospheric thickness variations beneath Australia on seismic anisotropy and mantle flow. *Geochemistry, Geophysics, Geosystems* **24**, doi:10.1029/2023gc011066 (2023).

54 de Laat, J. I. *et al.* Structure and evolution of the Australian plate and underlying upper mantle from waveform tomography with massive data sets. *Geophysical Journal International* **234**, 153-189, doi:10.1093/gji/ggad062 (2023).

55 Thiel, S., Reid, A., Heinson, G., Brand, K. & Li, L. Mantle-derived fluid flux controls Olympic Dam-style Fe oxide-Cu-Au mineralisation. *Scientific Reports* **16**, doi:10.1038/s41598-025-33477-7 (2026).

56 Ba, K., Gao, S. S., Song, J. & Liu, K. H. Seismic azimuthal anisotropy beneath a fast moving ancient continent: Constraints from shear wave splitting analysis in Australia. *Journal of Geophysical Research: Solid Earth* **128**, e2022JB025866, doi:https://doi.org/10.1029/2022JB025866 (2023).

57 Tietze, K., Thiel, S., Brand, K. & Heinson, G. Comparative 3D inversion of magnetotelluric phase tensors and impedances reveals electrically anisotropic base of Gawler Craton, South Australia. *Exploration Geophysics*, doi:10.1080/08123985.2023.2281615 (2023).

58 Li, Y., Jiang, H. T. & Yang, X. Z. Fluorine follows water: Effect on electrical conductivity of silicate minerals by experimental constraints from phlogopite. *Geochimica Et Cosmochimica Acta* **217**, 16-27, doi:10.1016/j.gca.2017.08.020 (2017).

59 Li, Y., Yang, X. Z., Yu, J. H. & Cai, Y. F. Unusually high electrical conductivity of phlogopite: the possible role of fluorine and geophysical implications. *Contrib Mineral Petr* **171**, doi:10.1007/s00410-016-1252-x (2016).

60 Thiel, S. & Heinson, G. Crustal imaging of a mobile belt using magnetotellurics: An example of the Fowler Domain in South Australia. *Journal of Geophysical Research: Solid Earth* **115**, doi:10.1029/2009jb006698 (2010).

61 Korsch, R. J., Doublier, M. P., Hagemann, S. G., Lisitsin, V. & Huston, D. L. Major crustal boundaries of Australia, and their significance in mineral systems targeting. *Ore geology reviews* **76**, 211-228, doi:10.1016/j.oregeorev.2015.05.010 (2016).

62 Heinson, G., Didana, Y., Soeffky, P., Thiel, S. & Wise, T. The crustal geophysical signature of a world-class magmatic mineral system. *Scientific reports* **8**, 10608-10606, doi:10.1038/s41598-018-29016-2 (2018).

63 Kennett, B. L. N., Salmon, M., Saygin, E. & Group, A. W. AusMoho: the variation of Moho depth in Australia. *Geophysical Journal International* **187**, 946-958, doi:10.1111/j.1365-246X.2011.05194.x (2011).

64 Roots, E. A. *et al.* Channelized metasomatism in Archean cratonic roots as a mechanism of lithospheric refertilization. *Nature Communications* **16**, doi:10.1038/s41467-025-62912-6 (2025).

65 Bologna, M. S. *et al.* Electrical structure of the lithosphere from Rio de la Plata Craton to Paraná Basin: Amalgamation of cratonic and refertilized lithospheres in SW Gondwanaland. *Tectonics* **38**, 77-94, doi:https://doi.org/10.1029/2018TC005148 (2019).

66 Bassin, C. G. L., Laske, G. & Masters, G. The current limits of resolution for surface wave tomography in North America. EOS Trans AGU 81:F897. *Eos* **81**, F897 (2000).

67 Lebedev, S. & Van Der Hilst, R. D. Global upper-mantle tomography with the automated multimode inversion of surface and S-wave forms. *Geophysical Journal International* **173**, 505-518, doi:10.1111/j.1365-246X.2008.03721.x (2008).

68 Wise, T., Pawley, M., Thiel, S., Dutch, R. & Anonymous. Geology, geophysics, geochemistry of a hidden Palaeoproterozoic ocean-continent transition in the northern Gawler Craton. *ASEG Extended Abstracts* **2018**, 1-5, doi:10.1071/ASEG2018abM3_1G (2018).

69 Fraser, G., Reid, A. & Stern, R. Timing of deformation and exhumation across the Karari Shear Zone, north-western Gawler Craton, South Australia. *Australian Journal of Earth Sciences* **59**, 547-570, doi:10.1080/08120099.2012.678586 (2012).

70 Pollett, A., Thiel, S., Bendall, B., Raimondo, T. & Hand, M. Mapping the Gawler Craton-Musgrave Province interface using integrated heat flow and magnetotellurics. *Tectonophysics* **756**, 43-56, doi:10.1016/j.tecto.2019.02.017 (2019).

71 Thomas, R. J., Hand, M. & Reid, A. Tectonic evolution of the Karari Shear Zone, northwestern Gawler Craton. *Precambrian Research* **166**, 123–138, doi:10.1016/j.precamres.2008.01.010 (2008).

72 Özaydin, S. & Selway, K. MATE: An analysis tool for the interpretation of magnetotelluric models of the mantle. *Geochemistry Geophysics Geosystems* **21**, doi:10.1029/2020gc009126 (2020).

73 Constable, S. SEO3: A new model of olivine electrical conductivity. *Geophysical Journal International* **166**, 435-437, doi:10.1111/j.1365-246X.2006.03041.x (2006).

74 Wang, D., Li, H., Yi, L. & Shi, B. The electrical conductivity of upper-mantle rocks: water content in the upper mantle. *Physics and Chemistry of Minerals* **35**, 157-162, doi:10.1007/s00269-007-0207-1 (2008).

75 Bettac, S. P., Unsworth, M. J., Pearson, D. G. & Craven, J. New constraints on the structure and composition of the lithospheric mantle beneath the Slave craton, NW Canada from 3-D magnetotelluric data-Origin of the Central Slave Mantle Conductor and possible evidence for lithospheric scale fluid flow. *Tectonophysics* **851**, doi:10.1016/j.tecto.2023.229760 (2023).

76 Steenstra, E. S. *et al.* Thermal Stability of F-Rich Phlogopite and K-Richterite During Partial Melting of Metasomatized Mantle Peridotite With Implications for Deep Earth Volatile Cycles. *Journal of Geophysical Research: Solid Earth* **129**, e2023JB028202, doi:https://doi.org/10.1029/2023JB028202 (2024).

77 Pommier, A. & Le-Trong, E. “SIGMELTS”: A web portal for electrical conductivity calculations in geosciences. *Computers & Geosciences* **37**, 1450-1459, doi:https://doi.org/10.1016/j.cageo.2011.01.002 (2011).

78 Foley, S. F. Rejuvenation and erosion of the cratonic lithosphere. *Nature Geoscience* **1**, 503-510, doi:10.1038/ngeo261 (2008).

79 Chen, C. F. *et al.* Sulfide-rich continental roots at cratonic margins formed by carbonated melts. *Nature* **637**, doi:10.1038/s41586-024-08316-w (2025).

80 Huizenga, J.-M. Thermodynamic modelling of a cooling C–O–H fluid–graphite system: implications for hydrothermal graphite precipitation. *Miner Deposita* **46**, 23-33, doi:10.1007/s00126-010-0310-y (2011).

81 Murphy, B. S., Huizenga, J. M. & Bedrosian, P. A. Graphite as an electrically conductive indicator of ancient crustal-scale fluid flow within mineral systems. *Earth*

and Planetary Science Letters **594**, 117700, doi:https://doi.org/10.1016/j.epsl.2022.117700 (2022).

82 Zhang, C. & Duan, Z. GFluid: An Excel spreadsheet for investigating C–O–H fluid composition under high temperatures and pressures. *Computers & Geosciences* **36**, 569-572, doi:https://doi.org/10.1016/j.cageo.2009.05.008 (2010).

83 Neumann, N., Sandiford, M. & Foden, J. Regional geochemistry and continental heat flow: implications for the origin of the South Australian heat flow anomaly. *Earth and Planetary Science Letters* **183**, 107-120, doi:https://doi.org/10.1016/S0012-821X(00)00268-5 (2000).

84 Chave, A. D. & Thomson, D. J. Bounded influence magnetotelluric response function estimation. *Geophys J Int* **157**, 988-1006, doi:10.1111/j.1365-246X.2004.02203.x (2004).

85 Chave, A. D. & Thomson, D. J. A bounded influence regression estimator based on the statistics of the hat matrix. *J R Stat Soc C-Appl* **52**, 307-322, doi:Doi 10.1111/1467-9876.00406 (2003).

86 Krieger, L. & Peacock, J. R. MTpy: A Python toolbox for magnetotellurics. *Computers & geosciences* **72**, 167-175, doi:10.1016/j.cageo.2014.07.013 (2014).

87 Mackie, R. L. & Madden, T. R. 3-Dimensional Magnetotelluric Inversion Using Conjugate Gradients. *Geophys J Int* **115**, 215-229, doi:DOI 10.1111/j.1365-246X.1993.tb05600.x (1993).

88 Rodi, W. & Mackie, R. L. Nonlinear conjugate gradients algorithm for 2-D magnetotelluric inversion. *Geophysics* **66**, 174-187, doi:Doi 10.1190/1.1444893 (2001).

89 Kuvshinov, A., Grayver, A., Tøffner-Clausen, L. & Olsen, N. Probing 3-D electrical conductivity of the mantle using 6 years of Swarm, CryoSat-2 and observatory magnetic data and exploiting matrix Q-responses approach. *Earth, Planets and Space* **73**, 67, doi:10.1186/s40623-020-01341-9 (2021).

Supplementary Files

This is a list of supplementary files associated with this preprint. Click to download.

- Heinson02102026Supp.pdf